

The amplitude mode in three-dimensional dimerized antiferromagnets

Yan Qi Qin,¹ B. Normand,² Anders W. Sandvik,³ and Zi Yang Meng¹

¹*Beijing National Laboratory for Condensed Matter Physics and
Institute of Physics, Chinese Academy of Sciences, Beijing 100190, China*

²*Laboratory for Neutron Scattering and Imaging,*

Paul Scherrer Institute, CH-5232 Villigen PSI, Switzerland

³*Department of Physics, Boston University, 590 Commonwealth Avenue, Boston, Massachusetts 02215, USA*

(Dated: October 18, 2016)

The amplitude (Higgs) mode is a ubiquitous collective excitation related to spontaneous breaking of a continuous symmetry. We combine quantum Monte Carlo (QMC) simulations with stochastic analytic continuation to investigate the dynamics of the amplitude mode in a three-dimensional dimerized quantum spin system. We characterize this mode by calculating the spin and dimer spectral functions near the quantum critical point, finding that both the energies and the intrinsic widths satisfy field-theoretical scaling predictions. While the line width of the spin response is close to that observed in neutron scattering experiments on TiCuCl_3 , the dimer response is significantly broader. Our results demonstrate that highly non-trivial dynamical properties are accessible by modern QMC and analytic continuation methods.

The spontaneous breaking of a continuous symmetry allows collective excitations of the direction and amplitude of the order parameter; for $O(N)$ symmetry, there are $N-1$ massless directional (Goldstone) modes and one massive amplitude mode [1–4]. In loose analogy with the Standard Model, the latter is often referred to as a Higgs mode. A strongly damped amplitude mode has been reported in two dimensions (2D) at the Mott transition of ultracold bosons [5] and at the disorder-driven superconductor–insulator transition [6, 7]. The amplitude mode is expected on theoretical grounds to be more robust in 3D, and, indeed, the cleanest observation of a “Higgs boson” in condensed matter is in the dimer quantum magnet TiCuCl_3 at its pressure-induced antiferromagnetic quantum phase transition (QPT) [8–10].

Below the upper critical number of space-time dimensions, which for an $O(N)$ model is $D_c = 4$, the amplitude mode is unstable, decaying primarily into pairs of Goldstone bosons [11–13]. In both 2D and 3D, the longitudinal dynamic susceptibility exhibits an infrared singularity due to the Goldstone modes [14], whose consequences for the visibility of the amplitude mode have been investigated extensively in 2D [15–17]. It was noted [14] that the scalar $O(N)$ -symmetric susceptibility remains uncontaminated by infrared contributions, which should permit the amplitude mode to be observed as a well-defined peak. The (3+1)D $O(3)$ case of TiCuCl_3 is at D_c and the amplitude mode is critically damped, meaning that its width is proportional to its energy [18]. This mode can be probed through the spin response (longitudinal susceptibility) by neutron spectroscopy, and measurements over a wide range of pressures reveal a rather narrow peak width of just 15% of the excitation energy [10]. The width-to-energy ratio is the key to the mode visibility, thus calling for unbiased numerical calculations in suitable model Hamiltonians.

In this Letter, we provide a systematic investigation of

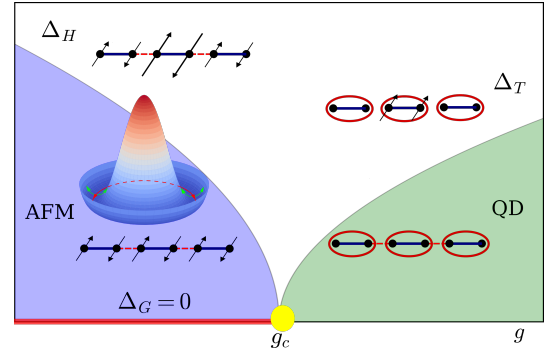


FIG. 1. Schematic representation of excitation processes and corresponding gaps in a dimerized antiferromagnet. The ratio $g = J'/J$ of the intra- and inter-dimer coupling constants controls a QPT from an AFM to a QD state. In the AFM phase, the excitations are two gapless spin waves (Goldstone modes, $\Delta_G = 0$) plus an amplitude mode at energy Δ_H , which correspond respectively to axial and radial fluctuations in the “Mexican hat” potential. In the QD phase, singlet-triplet dimer excitations have a gap Δ_T .

the dynamics and scaling of the amplitude mode at all coupling values across the QPT in a 3D dimerized spin-1/2 antiferromagnet, by performing large-scale stochastic series expansion quantum Monte Carlo (SSE-QMC) simulations and applying advanced stochastic analytic continuation (SAC) methods. Thus we provide an unbiased numerical demonstration that the amplitude mode is precisely critically damped and that its energy, width, and height obey field-theoretical predictions. Beyond these universal scaling forms, we quantify the nonuniversal width-to-energy ratios of the amplitude-mode peaks in the spin and dimer channels.

We consider the double-cubic geometry [19], which consists of two interpenetrating simple cubic lattices with nearest-neighbor Heisenberg exchange interactions $J_{ij} \vec{S}_i \cdot \vec{S}_j$, where $J_{ij} = J$ within each cubic lattice and

$J_{ij} = J'$ for inter-cube (intra-dimer) bonds. Increasing the ratio $g = J'/J$ drives a QPT where the ground state changes from a “renormalized classical” antiferromagnetic (AFM) state to a quantum disordered (QD) dimer-singlet state (Fig. 1). This transition is in the same universality class as the pressure-driven QPT in TiCuCl_3 . In a recent QMC analysis of the static properties of the double-cubic system [20], we established the quantum critical point (QCP) as $g_c = 4.83704(6)$ and quantified the logarithmic (log) scaling corrections expected near criticality in the AFM state at D_c .

We use SSE-QMC [21, 22] to measure both the spin-spin and dimer-dimer correlation functions in imaginary time; technical details may be found in Supplemental Material (SM) [23]. The former probes $S = 1$ excitations of the ground state (including the longitudinal mode) while the latter probes $S = 0$ (symmetric scalar [14–16]) excitations. We employ advanced SAC methods [24–29] to obtain high-resolution data for the spin and dimer spectral functions, and discuss the concepts and practicalities of this procedure in the SM [23]. Depending on the value of g , both spectral functions contain features arising from the Goldstone, amplitude, and triplon (gapped singlet-triplet) excitations. Henceforth we use the term “Higgs” as shorthand for the amplitude-mode contributions. The positions and gaps of these modes are represented schematically in Fig. 1.

Our simulations are performed on a system of $N = 2L^3$ sites at an inverse temperature $J\beta = 2L$, such that the low-temperature limit, $T \rightarrow 0$, is achieved as $L \rightarrow \infty$. The dynamical magnetic ($S = 1$) response is obtained from the spin correlation function

$$S(\mathbf{q}, \tau) = \langle S_{-\mathbf{q}}^z(\tau) S_{\mathbf{q}}^z(0) \rangle, \quad S_{\mathbf{q}}^z = \frac{1}{\sqrt{N}} \sum_{\mathbf{r}} e^{-i\mathbf{q} \cdot \mathbf{r}} S_{\mathbf{r}}^z, \quad (1)$$

where τ is the imaginary time in the Heisenberg representation of the operator. When analytically continued to real frequency, $S(\mathbf{q}, \tau)$ gives the dynamical structure factor, $S(\mathbf{q}, \omega)$, measured by inelastic neutron scattering. Our simulations contain no breaking of spin-rotation symmetry and thus do not separate the longitudinal and transverse components of the spectral function explicitly. The Higgs mode is contained in the longitudinal part, but the transverse part may contain both well-defined spin-wave or quantum-rotor modes and an excitation continuum that could obscure the Higgs contribution in the rotationally averaged $S(\mathbf{q}, \omega)$. However, unlike the 2D case [30], the transverse continuum is expected to be very small in 3D, especially at the staggered wave vector $\mathbf{q} = \mathbf{Q} = (\pi, \pi, \pi, \pi)$ on which we focus here (the last π corresponds to AFM ordering on each dimer).

The scalar ($S = 0$) dynamical response is obtained from the dimer correlation function at the zone center,

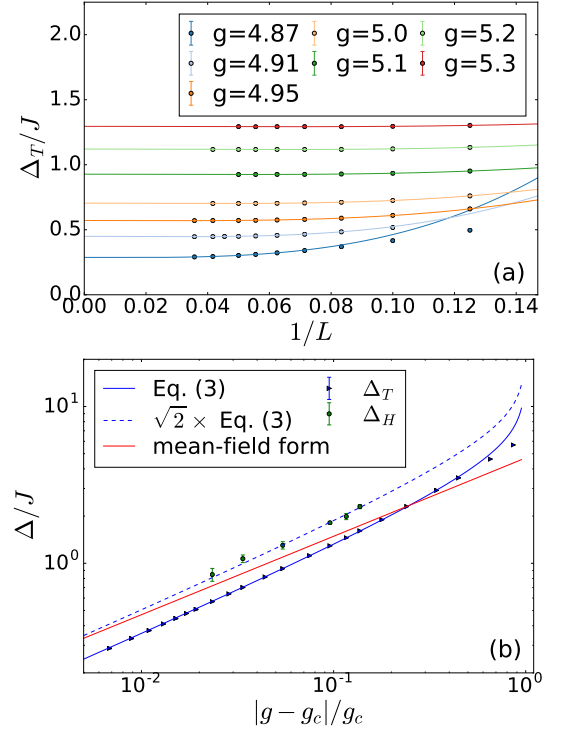


FIG. 2. (a) Extrapolation of the finite-size triplon gap for selected values of $g > g_c$ (QD phase). (b) Triplon gaps in the thermodynamic limit (blue triangles), shown vs $|g - g_c|/g_c$. The red line shows a pure mean-field (square-root) form, the blue line includes the log correction of Eq. (3) with fitted exponent $\hat{\nu} = 0.230(2)$, and green points show the extrapolated Higgs energy, Δ_H , obtained for values of $g < g_c$ (AFM phase) mirroring those used in panel (a). The blue dashed line is the log-corrected Δ_T result multiplied by $\sqrt{2}$.

$\mathbf{q} = \mathbf{\Gamma} = (0, 0, 0)$, which is given by

$$D(\mathbf{\Gamma}, \tau) = \langle B_{\mathbf{\Gamma}}(\tau) B_{\mathbf{\Gamma}}(0) \rangle, \quad B_{\mathbf{\Gamma}} = \frac{1}{\sqrt{N}} \sum_{\mathbf{r}} B_{\mathbf{r}}, \quad (2)$$

where $B_{\mathbf{r}} = \mathbf{S}_{\mathbf{r}1} \cdot \mathbf{S}_{\mathbf{r}2} - \langle \mathbf{S}_{\mathbf{r}1} \cdot \mathbf{S}_{\mathbf{r}2} \rangle$ is the inter-cube dimer operator and the sum includes only one of the cubes ($\mathbf{r} = \mathbf{r}1$). This quantity was also employed in a recent study of the (2+1)D (bilayer) version of the double-cubic system [31]. The real-frequency quantity $D(\mathbf{\Gamma}, \omega)$ may be probed experimentally by Raman scattering [32, 33].

As an alternative to SAC, one may also attempt to extract gap information by a direct analysis of the large- τ exponential decays of the correlation functions [34, 35]. Considering the spin sector, the smallest singlet-triplet gap occurs at $\mathbf{q} = \mathbf{Q}$ and in the QD phase $S(\mathbf{Q}, \tau)$ is dominated by the triplon mode. In the AFM phase, this gap corresponds to the lowest Goldstone mode, which has only a finite-size energy proportional to $1/N$. Thus $S(\mathbf{Q}, \tau)$ decays very slowly with τ in this case and the dominant Goldstone contribution threatens to obscure the Higgs contribution [14–17, 36]. Examples of imaginary-time data for $S(\mathbf{Q}, \tau)$ and gap extractions are presented in the SM [23].

We begin a detailed analysis of our results by discussing the triplon gap in the QD phase ($g > g_c$). For a given value of g , we extract the finite-size gap, $\Delta_T(L)$, from $S(\mathbf{Q}, \tau)$ for a range of system sizes. As shown in Fig. 2(a), $\Delta_T(L)$ decreases with increasing L for every g value before converging to the thermodynamic limit. We extrapolate to obtain $\Delta_T(g)$ using a cubic-order polynomial fit in $1/L$, and show the results as a function of the separation, $|g - g_c|/g_c$, from the QCP in Fig. 2(b).

In the ϕ^4 theory for an $O(N)$ order parameter, at $D = D_c$ one expects physical quantities to exhibit power-law scaling with mean-field critical exponents, but with multiplicative log corrections [3, 37], which have now been found in a number of recent studies [20, 38, 39]. The scaling form of the triplon gap can be obtained directly from the correlation length ($\Delta \sim 1/\xi$), whence

$$\Delta_T \sim (|g - g_c|/g_c)^\nu \ln^{-\hat{\nu}}(|g - g_c|/g_c), \quad (3)$$

with $\nu = 1/2$ [3, 40] and $\hat{\nu} = (N + 2)/2(N + 8)$ from perturbative renormalization-group calculations [37, 41], i.e. $\hat{\nu} = 5/22 \approx 0.227$ for $N = 3$. It is clear from Fig. 2(b) that Eq. (3) describes the data far better than the pure mean-field form and, by performing an optimized fit [20] with $\hat{\nu}$ as a free parameter, we deduce the exponent $\hat{\nu} = 0.230(2)$, fully consistent with the theoretical prediction.

To study the amplitude mode in detail, we analyze the spectral functions $S(\mathbf{Q}, \omega)$ and $D(\mathbf{\Gamma}, \omega)$ in the AFM phase ($g < g_c$) near g_c . Figure 3 shows both quantities at $g = 4.724$ for several system sizes. Because SSE-QMC calculations of $D(\mathbf{\Gamma}, \tau)$ are significantly more demanding (see [23]), these are restricted to $L \leq 16$, whereas for $S(\mathbf{Q}, \tau)$ we access sizes up to $L = 24$.

$S(\mathbf{Q}, \omega)$ [Fig. 3(a)] is dominated by the Goldstone contribution, whose spectral weight is proportional to N at $T = 0$ (becoming the magnetic Bragg peak as $L \rightarrow \infty$), but the Higgs mode nevertheless appears as a clearly resolved finite-energy peak (as also observed experimentally in TiCuCl_3 [9, 10]). Because longitudinal and transverse fluctuations cannot be distinguished at g_c , the Higgs spectral weight also diverges as $g \rightarrow g_c$. Away from g_c , it remains as a finite-energy mode with convergent spectral weight. Because the finite-size Goldstone peak scales in energy as $1/L^3$, it remains subject to thermal broadening in our analysis (where $T \propto 1/L$); in contrast, we have confirmed that the Higgs peak is not affected by thermal broadening. The peak widths are also stable with respect to increasing the amount of QMC data, and any artificial broadening arising from the SAC procedures should therefore be minimal.

In $D(\mathbf{\Gamma}, \omega)$ [Fig. 3(b)], the Higgs contribution is the distinctive low-energy peak, which is separated by a region of suppressed spectral weight from a broad maximum representing lattice-scale fluctuations. In the thermodynamic limit, one expects an infrared tail with a characteristic scaling $D(\mathbf{\Gamma}, \omega) \propto \omega^4$ [14], but this is too weak to observe by SAC and with the available system sizes.

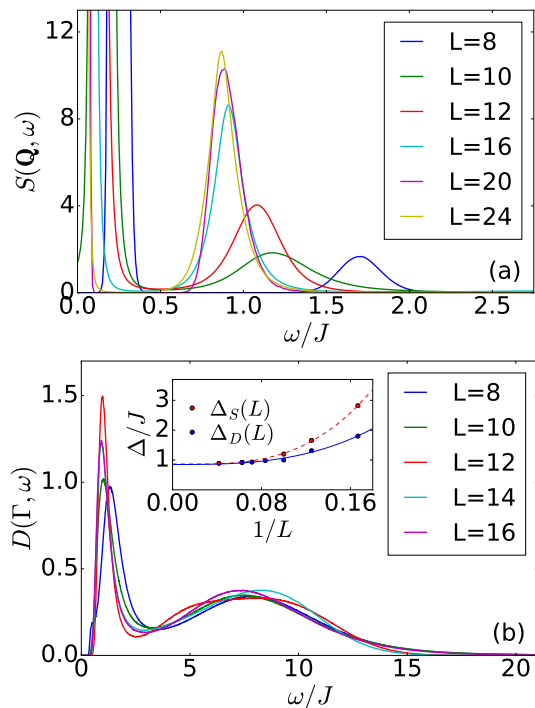


FIG. 3. (a) $S(\mathbf{Q}, \omega)$ and (b) $D(\mathbf{\Gamma}, \omega)$ obtained by SAC at $g = 4.724$ for different system sizes. The large low-energy (Goldstone) peak in panel (a) is cut off in order to show the secondary (Higgs) peak. The lower peak in panel (b) is the Higgs mode. The positions of both Higgs contributions converge with increasing L to the same thermodynamic limit, as shown in the inset of panel (b). No spectral features were discernible outside the energy ranges shown.

We observe good convergence with increasing L in each of $S(\mathbf{Q}, \tau)$ and $D(\mathbf{\Gamma}, \tau)$, and further that the peak positions of each quantity also converge to the same value, as shown in the inset of Fig. 3(b). This consistency between the $S = 0$ and $S = 1$ excitations provides strong confirmation that the peaks in the SAC spectral functions do indeed correspond to the Higgs mode. We have confirmed by a bootstrapping analysis that the fluctuations in the height and width of the lower $D(\mathbf{\Gamma}, \tau)$ peak for $L \geq 10$ in Fig. 3 reflect statistical errors. Our system sizes are sufficient for a reliable study of the $L \rightarrow \infty$ limit in both sectors up to $g \approx g_c - 0.1$.

In Fig. 2(b) we compare the extrapolated Higgs energies in the AFM phase with the triplet gaps in the QD phase at the same distance, $|g - g_c|/g_c$, from the QCP. The predicted $\sqrt{2}$ ratio [36, 38, 40] between Δ_H and Δ_T is clearly obeyed over this rather broad coupling range. We stress that this relation implies the presence of equivalent multiplicative log corrections [Eq. (3)] to both Δ_T in the QD phase and Δ_H on the AFM side. We do not observe any deviations from the $\sqrt{2}$ relationship up to $|g - g_c|/g_c = 0.14$, even though it is not exact [38].

To investigate the scaling properties of the spectral functions as the QCP is approached, we normalize ω

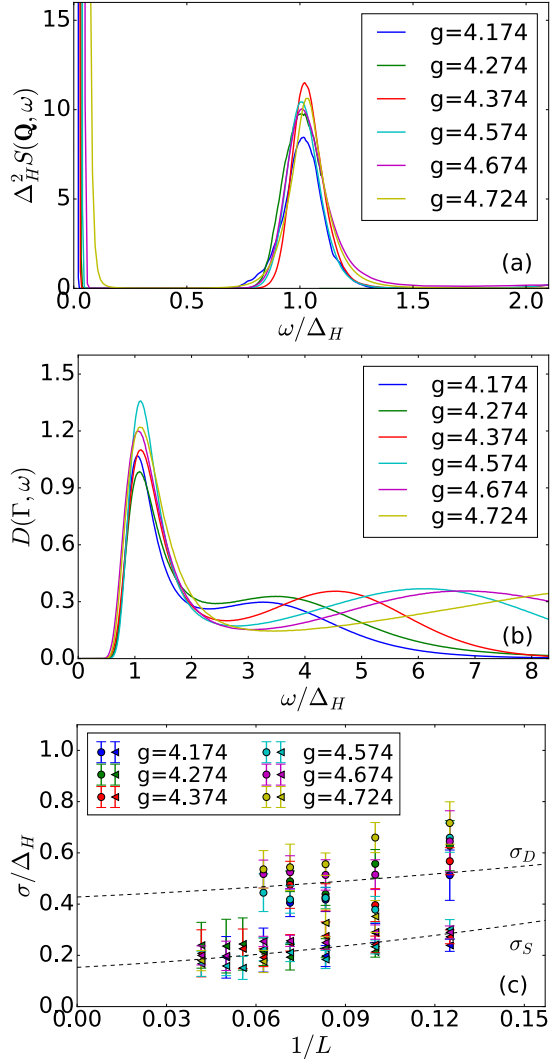


FIG. 4. (a) The scaled spectrum $\Delta_H^2 S(\mathbf{Q}, \omega/\Delta_H)$ calculated with $L = 24$ for a range of g values. (b) $D(\Gamma, \omega/\Delta_H)$ calculated with $L = 16$. (c) Scaled peak widths shown vs $1/L$. Circles and triangles are obtained from $D(\Gamma, \omega/\Delta_H)$ and $S(\mathbf{Q}, \omega/\Delta_H)$, respectively. The dashed curves are second-order polynomial fits to error-weighted average widths.

by the $L \rightarrow \infty$ Higgs gap; results for $S(\mathbf{Q}, \omega/\Delta_H)$ and $D(\Gamma, \omega/\Delta_H)$ are shown respectively in Figs. 4(a) and 4(b) for the largest system sizes considered in each case. The amplitude-mode contributions to both the spin and dimer spectral functions exhibit near-ideal data collapse when scaled in this way. The collapse of the peaks indicates that our data represent the the quantum critical regime in the thermodynamic limit, and the proportionality of the peak widths to Δ_H demonstrates that the Higgs mode indeed is critically damped.

A universal scaling form for the scalar susceptibility (dimer spectral function) in the vicinity of the QCP,

$$D(\Gamma, \omega) \sim \Delta_H^{d+z-2/\nu} \Phi(\omega/\Delta_H), \quad (4)$$

has been derived perturbatively in $1/N$ for the $O(N)$

model [15–17] and also by using the $4 - \epsilon$ expansion [36]. In (3+1)D with $z = 1$, we expect $D(\Gamma, \omega) = \Phi(\omega/\Delta_H)$, which is fully consistent with the data in Fig. 4(b). This type of scaling has been documented in (2+1)D for both $O(2)$ [16, 17, 42–44] and $O(3)$ models [31, 44], but to our knowledge Fig. 4(b) constitutes its only unbiased numerical demonstration in (3+1)D. For $S(\mathbf{Q}, \omega/\Delta_H)$ we obtain data collapse by appealing to the result [9] that the integrated spectral weight diverges as $1/\Delta_H$ when $g \rightarrow g_c$, which requires a rescaling by Δ_H^2 [Fig. 4(a)]. We may expect log corrections here as well [18], but, within the range of g -values considered, their effects on the data collapse are not detectable.

For a quantitative analysis of the spin and dimer Higgs widths, σ_S and σ_D , in Fig. 4(c) we show the size-dependence of the width-to-energy ratios, using the full width at half-maximum height of the peaks. The error bars obtained by bootstrapping are significant, but it is clear that (i) the size dependence of σ_S/Δ_H and σ_D/Δ_H is weak, (ii) the dependence on g is weak, and (iii) the dimer peaks are broader than the spin peaks by a factor of ≈ 3 . To mitigate the large error bars, we use error-weighted averages of the width ratios obtained from all the g values at each L , and fit these to a quadratic polynomial in $1/L$, as shown with the dashed curves in Fig. 4(c). This way we obtain estimates $\sigma_S/\Delta_H = 0.15(4)$ and $\sigma_D/\Delta_H = 0.43(6)$ of the near-critical ratios.

Remarkably, our SAC value for σ_S/Δ_H on the double-cubic lattice is in excellent agreement with the neutron scattering results for TiCuCl_3 near its QCP [9, 10, 18]. Given the quite different lattices and couplings, this result mandates a deeper investigation of possible reasons for a very weak dependence on microscopic details. The much larger value of σ_D/Δ_H may reflect the different states probed by the two spectral functions. The Higgs part of the $S = 1$ spectrum can be considered as the combination of a quantum-rotor excitation with the elementary $S = 0$ Higgs mode (probed by the dimer spectrum), and indeed the finite-size spin peak lies higher in energy than the dimer peak [inset, Fig. 3(b)]. This composite nature of the $S = 1$ excitation implies different matrix-element effects in the peak shapes, which are also evident in the different scaling forms of the peak areas in Fig. 4.

In summary, we have used large-scale quantum Monte Carlo simulations to investigate the quantum critical dynamics of the amplitude (Higgs) mode in a 3D dimerized antiferromagnet. Our work demonstrates that modern SAC methods are capable of resolving complex spectral functions, here with two peaks and non-trivial scaling behavior of both the peak widths and heights. Our results not only verify the scaling predictions based on field-theory methods but also provide line-width information and nonuniversal factors that lie beyond current analytical treatments. The type of calculations reported here can be performed for different momenta, to study the dispersion of the amplitude mode and the evolution of

its width in the spin and dimer sectors, as well as for the lattice geometry and exchange couplings of TiCuCl_3 .

Acknowledgments.—We would like to thank Stefan Wessel for communicating results of a related investigation [45] prior to publication, Hui Shao for discussions and related work on the SAC method, and Oleg Sushkov for discussions. Numerical calculations were performed on the Tianhe-1A platform at the National Supercomputer Center in Tianjin. YQQ and ZYM acknowledge support from the Ministry of Science and Technology of China under Grant No. 2016YFA0300502, the National Science Foundation of China under Grant Nos. 11421092 and 11574359, and the National Thousand-Young-Talents Program of China. YQQ would like to thank the Condensed Matter Theory Visitors Program of Boston University. AWS was supported by the NSF under Grant No. DMR-1410126 and would also like to thank the Institute of Physics of the Chinese Academy of Sciences for visitor support.

-
- [1] J. Goldstone, A. Salam, and S. Weinberg, *Phys. Rev.* **127**, 965 (1962).
 - [2] P. W. Higgs, *Phys. Rev. Lett.* **13**, 508 (1964).
 - [3] J. Zinn-Justin, *Quantum field theory and critical phenomena* (Oxford, Clarendon Press, 2002).
 - [4] S. Sachdev, *Quantum phase transitions* (Cambridge University Press, 2011).
 - [5] M. Endres, T. Fukuhara, D. Pekker, M. Cheneau, P. Schauss, C. Gross, E. Demler, S. Kuhr, and I. Bloch, *Nature* **487**, 454 (2012).
 - [6] M. Swanson, Y. L. Loh, M. Randeria, and N. Trivedi, *Phys. Rev. X* **4**, 021007 (2014).
 - [7] D. Sherman, U. S. Pracht, B. Gorshunov, S. Poran, J. Jesudasan, M. Chand, P. Raychaudhuri, M. Swanson, N. Trivedi, A. Auerbach, M. Scheffler, A. Frydman, and M. Dressel, *Nat Phys* **11**, 188192 (2015).
 - [8] C. Rüegg, A. Furrer, D. Sheptyakov, T. Strässle, K. W. Krämer, H.-U. Güdel, and L. Mélési, *Phys. Rev. Lett.* **93**, 257201 (2004).
 - [9] C. Rüegg, B. Normand, M. Matsumoto, A. Furrer, D. F. McMorrow, K. W. Krämer, H. U. Güdel, S. N. Gvasaliya, H. Mutka, and M. Boehm, *Phys. Rev. Lett.* **100**, 205701 (2008).
 - [10] P. Merchant, B. Normand, K. W. Kramer, M. Boehm, D. F. McMorrow, and C. Ruegg, *Nat Phys* **10**, 373 (2014).
 - [11] S. Sachdev, *Phys. Rev. B* **59**, 14054 (1999).
 - [12] W. Zwerger, *Phys. Rev. Lett.* **92**, 027203 (2004).
 - [13] N. Dupuis, *Phys. Rev. E* **83**, 031120 (2011).
 - [14] D. Podolsky, A. Auerbach, and D. P. Arovas, *Phys. Rev. B* **84**, 174522 (2011).
 - [15] D. Podolsky and S. Sachdev, *Phys. Rev. B* **86**, 054508 (2012).
 - [16] S. Gazit, D. Podolsky, and A. Auerbach, *Phys. Rev. Lett.* **110**, 140401 (2013).
 - [17] S. Gazit, D. Podolsky, A. Auerbach, and D. P. Arovas, *Phys. Rev. B* **88**, 235108 (2013).
 - [18] Y. Kulik and O. P. Sushkov, *Phys. Rev. B* **84**, 134418 (2011).
 - [19] S. Jin and A. W. Sandvik, *Phys. Rev. B* **85**, 020409 (2012).
 - [20] Y. Q. Qin, B. Normand, A. W. Sandvik, and Z. Y. Meng, *Phys. Rev. B* **92**, 214401 (2015).
 - [21] A. W. Sandvik, *Phys. Rev. B* **59**, R14157 (1999).
 - [22] O. F. Syljuåsen and A. W. Sandvik, *Phys. Rev. E* **66**, 046701 (2002).
 - [23] Supplemental Material following the main paper.
 - [24] A. W. Sandvik, *Phys. Rev. B* **57**, 10287 (1998).
 - [25] K. S. D. Beach, [arXiv:cont-mat/0403055](https://arxiv.org/abs/cont-mat/0403055).
 - [26] O. F. Syljuåsen, *Phys. Rev. B* **78**, 174429 (2008).
 - [27] S. Fuchs, T. Pruschke, and M. Jarrell, *Phys. Rev. E* **81**, 056701 (2010).
 - [28] A. W. Sandvik, [arXiv:1502.06066](https://arxiv.org/abs/1502.06066).
 - [29] H. Shao and A. W. Sandvik (unpublished).
 - [30] A. W. Sandvik and R. R. P. Singh, *Phys. Rev. Lett.* **86**, 528 (2001).
 - [31] M. Lohöfer, T. Coletta, D. G. Joshi, F. F. Assaad, M. Vojta, S. Wessel, and F. Mila, *Phys. Rev. B* **92**, 245137 (2015).
 - [32] P. A. Fleury and R. Loudon, *Phys. Rev.* **166**, 514 (1968).
 - [33] B. S. Shastry and B. I. Shraiman, *Phys. Rev. Lett.* **65**, 1068 (1990).
 - [34] A. Sen, H. Suwa, and A. W. Sandvik, *Phys. Rev. B* **92**, 195145 (2015).
 - [35] H. Suwa, A. Sen, and A. W. Sandvik, *Phys. Rev. B* **94**, 144416 (2016).
 - [36] Y. T. Katan and D. Podolsky, *Phys. Rev. B* **91**, 075132 (2015).
 - [37] R. Kenna, *Nucl. Phys. B* **691**, 292 (2004).
 - [38] H. D. Scammell and O. P. Sushkov, *Phys. Rev. B* **92**, 220401 (2015).
 - [39] D.-R. Tan and F.-J. Jiang, [arXiv:1608.03835](https://arxiv.org/abs/1608.03835).
 - [40] S. Sachdev, [arXiv:0901.4103](https://arxiv.org/abs/0901.4103).
 - [41] R. Kenna, in *Order, Disorder and Criticality. Vol. III*, edited by Y. Holovatch (World Scientific, Singapore, 2012).
 - [42] L. Pollet and N. Prokof'ev, *Phys. Rev. Lett.* **109**, 010401 (2012).
 - [43] K. Chen, L. Liu, Y. Deng, L. Pollet, and N. Prokof'ev, *Phys. Rev. Lett.* **110**, 170403 (2013).
 - [44] F. Rose, F. Léonard, and N. Dupuis, *Phys. Rev. B* **91**, 224501 (2015).
 - [45] M. Lohöfer and S. Wessel (unpublished).
 - [46] A. W. Sandvik and J. Kurkijärvi, *Phys. Rev. B* **43**, 5950 (1991).
 - [47] A. W. Sandvik, *J. Phys. A: Math. Gen* **25**, 3667 (1992).
 - [48] M. Jarrell and J. Gubernatis, *Phys. Rep.* **269**, 133 (1996).
 - [49] D. Bergeron and A.-M. S. Tremblay, *Phys. Rev. E* **94**, 023303 (2016).
-

SUPPLEMENTAL MATERIAL

The amplitude mode in three-dimensional dimerized antiferromagnets

Y. Q. Qin, B. Normand, A. W. Sandvik, and Z. Y. Meng

Here we provide the technical details concerning our computations of imaginary-time spin and dimer correlation functions (Sec. SI), of the stochastic analytic continuation method for extracting the full real-frequency spectral functions (Sec. SII), and of gap extraction from the decay of the measured correlation functions at long imaginary times (Sec. SIII).

SI. Evaluation of dynamic correlation functions in SSE-QMC

We wish to compute the product of two operators, one of which is displaced in imaginary time,

$$\hat{O}_2(\tau)\hat{O}_1(0) = e^{\tau\hat{H}}\hat{O}_2e^{-\tau\hat{H}}\hat{O}_1. \quad (\text{S1})$$

Within SSE-QMC [21, 22, 46, 47], the exponential functions are Taylor-expanded, whereupon the time displacement is converted into a sum over the separations m between states propagated by m operators in the

importance-sampled operator strings originating from the Taylor expansion of the density matrix, $\exp(-\beta H)$. Here we present the relevant formulas in order to make some comments concerning the implementation of the method, and refer to the papers cited above for details of the SSE scheme and the origin of these formulas.

If the operators \hat{O}_1 and \hat{O}_2 are terms of the Hamiltonian (for example the dimer operators in the present case, which are Heisenberg exchange operators), for a given operator string one has [47]

$$\langle \hat{O}_1(\tau)\hat{O}_2(0) \rangle = \left\langle \sum_{m=0}^{n-2} \frac{\tau^m(\beta-\tau)^{n-m-2}}{\beta} \frac{(n-1)!}{(n-m-2)!m!} N(O_1, O_2; m) \right\rangle, \quad (\text{S2})$$

where n is the expansion order of the SSE configuration and $N(O_1, O_2; m)$ is the number of times the two operators are separated by m other operators in the string. If the two operators are diagonal in the basis of the SSE expansion, the correlation function can be written as

$$\langle \hat{O}_1(\tau)\hat{O}_2(0) \rangle = \left\langle \sum_{p=0}^{n-1} \sum_{m=0}^n \frac{\tau^m(\beta-\tau)^{n-m}}{\beta^n} \frac{(n-1)!}{(n-m)!m!} O_1(|p\rangle) O_2(|p+m\rangle) \right\rangle, \quad (\text{S3})$$

where $|p\rangle$ is the state propagated by p operators relative to a stored SSE state.

In the above expressions for the correlation functions, the prefactors of $N(O_1, O_2; m)$ or $O_1(|p\rangle)O_2(|p+m\rangle)$ are strongly peaked at $m \approx n\tau/\beta$, and it is therefore not necessary to evaluate the full sums over m ; for a given τ , a pre-computed m -range of sufficient width, meaning one containing approximately \sqrt{n} operators, can be used. Nevertheless, these summations are time-consuming and can often dominate the computational effort. In Ref. [31], a modified kernel was introduced in the analytic continuation to allow a different discretization of the correlation function (S2) used for the dimer correlations. Here we choose to use the full form, thus avoiding a potential loss of frequency resolution due to the further convolution im-

plied within the modified kernel. In order to ensure that the most time-consuming measurements are not carried out more often than necessary, by minimizing autocorrelations, we separate our measurements of the dimer-dimer correlation function by L SSE update sweeps.

Because spin-spin correlations are diagonal in the SSE basis, we can adopt a different and faster approach than the form (S3). We use a time-sliced form of the density matrix,

$$e^{-\beta H} = \prod_{l=1}^M e^{-\Delta H}, \quad \Delta = \beta/M, \quad (\text{S4})$$

and carry out the SSE simulations with each of the time slices, $e^{-\Delta H}$, expanded individually. This allows easy access to all correlation functions of diagonal operators sep-

arated by times that are multiples of the step Δ , simply by measuring the correlations in the propagated states at the boundaries between time slices.

In most cases we use a quadratic time grid, instead of the uniform grid normally used, with the times in the set $\{\tau_i\}$ of the form $\tau_i = \Delta i^2$ for $i = 0, 1, 2, \dots$. This kind of grid is useful when the inverse temperature, β , is large, as it gives access to both short and long times with a reasonably small set of times (typically numbering in tens rather than hundreds) for which the covariance matrix [48] required in analytic continuation can be computed properly. In Fig. S1 we show examples of the spin correlation functions in the QD and AFM phases, whose analysis we discuss in Secs. SII and SIII.

SII. STOCHASTIC ANALYTIC CONTINUATION

The imaginary-time correlation function of an operator \hat{O} , $G(\tau) = \langle \hat{O}(\tau) \hat{O}(0) \rangle$, is related to a corresponding spectral function, $A(\omega)$, according to

$$G(\tau) = \int_{-\infty}^{\infty} d\omega A(\omega) K(\tau, \omega), \quad (\text{S5})$$

where the kernel, $K(\tau, \omega)$, depends on the type of the spectral function. We wish to deduce the spectral function normally referred to as the dynamic structure factor (for the spin or dimer operator, as defined in the main text), which has the spectral representation

$$A(\omega) = \frac{1}{\pi} \sum_n e^{-\beta E_n} \sum_m |\langle m | \hat{O} | n \rangle|^2 \delta(\omega - E_n + E_m) \quad (\text{S6})$$

in terms of the energy eigenvalues and the corresponding matrix elements of the operator \hat{O} .

For the bosonic case studied here, the spectra at positive and negative frequencies obey the relation $A(-\omega) = e^{-\beta\omega} A(\omega)$, whence one may restrict the integral in Eq. (S5) to positive frequencies by using the kernel

$$K(\tau, \omega) = \frac{1}{\pi} (e^{-\tau\omega} + e^{-(\beta-\tau)\omega}). \quad (\text{S7})$$

The normalization of the spectrum can then be expressed as

$$G(0) = \int_0^{\infty} d\omega A(\omega) K(\tau=0, \omega). \quad (\text{S8})$$

In the version of the SAC method used here [29], we adopt the normalization $G(0) = 1$ [and later multiply the final spectrum by the original value of $G(0)$] in order to work with a spectral function that is itself normalized to unity on the positive frequency axis, i.e. without being multiplied by the kernel (S7). We therefore define

$$B(\omega) = A(\omega)(1 + e^{-\beta\omega}), \quad (\text{S9})$$

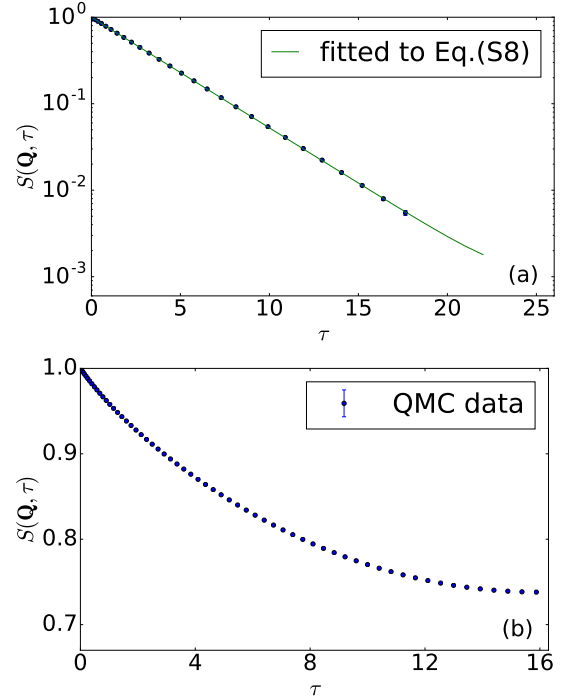


FIG. S1. Dynamical spin correlation functions for double-cubic systems with (a) $L = 24$ in the QD phase at $g = 4.87$ and (b) $L = 16$ in the AFM phase at $g = 4.724$. A quadratic grid of imaginary times, $\tau_i = \Delta i^2$, $i = 0, 1, 2, \dots$, was used in both cases and the inverse temperature was $\beta = 2L$. In panel (a), an almost pure exponential decay is observed and the gap is readily extracted from Eq. (S15) of Sec. SIII, giving $\Delta_T = 0.3028(1)$ (with the error bar estimated by bootstrapping). The spectral functions obtained by analytic continuation are shown in the corresponding panels of Fig. S2.

with normalization

$$\int_0^{\infty} d\omega B(\omega) = 1. \quad (\text{S10})$$

Using a modified kernel,

$$\bar{K}(\tau, \omega) = \frac{1}{\pi} \frac{e^{-\tau\omega} + e^{-(\beta-\tau)\omega}}{1 + e^{-\beta\omega}}, \quad (\text{S11})$$

the relationship between $B(\omega)$ and $G(\tau)$, normalized such that $G(0) = 1$, is

$$G(\tau) = \int_0^{\infty} d\omega B(\omega) \bar{K}(\tau, \omega). \quad (\text{S12})$$

Working with a set $\{\tau_i\}$ of imaginary time points, for which the values $G(\tau_i)$ and the accompanying covariance matrix, C_{ij} , have been computed using QMC simulations, our aim is to invert the integral relation (S12) numerically to acquire $B(\omega)$, and then to obtain $A(\omega)$ from Eq. (S9).

To carry out the analytic continuation, we use a variant [29] of the SAC approach [24–28], where a chosen

parameterization of the spectrum, typically using a large number of δ -functions, is sampled in a Monte Carlo simulation using a probability distribution

$$P(B) \propto \exp(-\chi^2/2\Theta), \quad (\text{S13})$$

where Θ is a fictitious temperature and thus χ^2 plays the role of an energy if the system is regarded as a problem in statistical mechanics. It has been demonstrated [25] that when this formulation is treated in a mean-field-type approximation, it reduces to the more commonly used Maximum Entropy (ME) method [48]. In general, one expects SAC to resolve finer details of the spectrum than ME, because it takes into account fluctuations around the mean-field solution, at the price of requiring long sampling times in certain cases (Refs. [27] and [49] contain some discussion of this point). The most recent variant of the method [29], which we deploy here, reduces these sampling times considerably, typically delivering simple single-peak spectral functions in a few minutes or less, when running on a single core, and more complicated spectra, such as the cases with two well-separated peaks that we consider here, in under an hour.

The sampling space is a large number, N_ω , of movable δ -functions placed on a frequency grid with a spacing Δ_ω sufficiently fine as to be regarded in practice as a continuum (e.g., $\Delta_\omega = 10^{-5}$). The number N_ω can range from of the order 100 for spectrums with little structure to 10^4 or more more complicated spectra. The optimal number also depends on the quality (statistical errors) of the QMC data, with better data requiring larger N_ω for efficient sampling.

At a given instant, the frequency of the i th δ -function is ω_i , which is an integer multiple of Δ_ω . A sweep consisting of N_ω moves of the type $\omega_r \rightarrow \omega'_r$ is performed, with r chosen randomly and the size of the change generated randomly within a window such that approximately half of the updates are accepted. The spectrum is accumulated in a histogram whose bin size is typically much larger than Δ_ω , and is chosen such that the features of the spectrum can be clearly resolved.

In the simplest case, the amplitudes of the δ -functions are all the same, $b_i = 1/N_\omega$, with their value corresponding to a spectrum $B(\omega)$ normalized to unity as discussed above. We stress that these amplitudes do not have to be changed, and a peak in the spectrum corresponds only to a high average density of δ -functions within a corresponding region. We also carry out simultaneous updates of more than one δ -function, a technique we will discuss in detail elsewhere [29]. The constant amplitudes are intended to reduce the amount of entropic bias [28] in the spectrum, and tests indicate that this development does indeed improve the fidelity of the method.

A further refinement is to not use the same amplitude for all δ -functions, but to generate a range of varying amplitudes, such as $b_i \propto i$ (with a prefactor chosen to satisfy the standard normalization), and this is the method

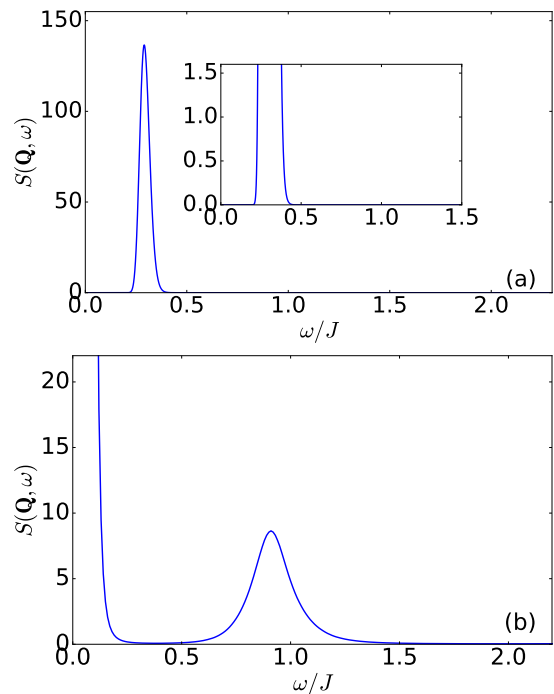


FIG. S2. Spectral functions obtained using the SAC method with the imaginary-time data shown in the corresponding panels of Fig. S1. There is no significant spectral weight beyond the frequency ranges shown.

we employ throughout the current analysis. These amplitudes are kept constant during the sampling process and, because there are no constraints on the locations of the δ -functions, small amplitudes can migrate to areas with lower spectral weight. As long as N_ω is sufficiently large, we find no differences in the final averaged spectrum between the methods of uniform or varying amplitudes. However, the sampling efficiency is increased in the method of varying amplitudes, especially if we include an amplitude update of two δ -functions of the type $b'_i = b_j$, $b'_j = b_i$, with i and j chosen randomly among all the δ -functions. When sampling spectra with two or more peaks, this update causes considerable improvements in the efficiency of transferring weight between peaks.

An important issue in SAC is how to select the sampling temperature, Θ . The general situation is that a very low Θ freezes the spectrum close to a stable or metastable χ^2 minimum, while a high Θ leads to large χ^2 values, i.e. poor fits to the QMC data for $G(\tau)$. There is a range of Θ over which the average χ^2 value is small but the fluctuations are significant, and cause a smoothing of the spectrum. There is no agreement on exactly how Θ should be chosen, but in general the different schemes proposed in the literature produce very similar results. This issue is similar to the various ways in which the entropic weighting of the spectrum can be chosen in the ME method [48, 49].

Here we adopt a simple temperature-adjustment scheme devised in Ref. [29], where a simulated annealing procedure is first carried out to find the minimum value χ_{\min}^2 (in practice this is actually a value close to the minimum, as it may be very difficult to reach the exact global minimum of χ^2). After this initial step, Θ is adjusted so that the average χ^2 during the final sampling process for collecting the spectrum satisfies the criterion

$$\langle \chi^2 \rangle \approx \chi_{\min}^2 + \sqrt{2N_\tau}, \quad (\text{S14})$$

where N_τ is the number of time points in the QMC dataset for $G(\tau)$. With N_τ replaced by N_{dof} (the number of degrees of freedom in a simple fitting procedure) the square-root term would be exactly the standard deviation of the χ^2 distribution. With the spectrum constrained to positive frequencies, the number of degrees of freedom is not simply the difference $N_\tau - N_\omega$, because the sampling parameters, which here are the N_ω frequencies, cannot be considered as independent variables (we note that typically $N_\omega \gg N_\tau$ so that N_{dof} from the naive definition would be negative and therefore meaningless). We therefore use instead the quantity $\sqrt{2N_\tau}$, which typically will be one to two standard deviations of the distribution. This level of noise then corresponds roughly to the removal of distortions due to “fitting to the statistical errors”. In practice, we find the criterion (S14) to produce excellent spectra in tests both on synthetic imaginary-time data and on actual QMC results for systems with known spectral functions [29].

We conclude this discussion by showing spectral functions obtained with the SAC method applied to the imaginary-time data in Fig. S1. In Fig. S2(a), where the system is in the QD phase, only a single narrow triplon peak is resolved, corresponding to the essentially pure exponential decay seen in Fig. S1(a). By contrast, when the system is in the AFM phase, we observe the two peaks shown in Fig. S2(b), the Goldstone mode at $\omega \propto 1/N$ and a smaller peak at higher frequency corresponding to the amplitude mode, the scaling properties of which are discussed in the main paper.

SIII. DOMINANT-MODE FITTING

If a spectral function, $A(\omega)$, contains a single δ -function, the corresponding imaginary-time correlation function, $G(\tau)$, decays exponentially at $T = 0$, with the decay constant being the inverse of the gap, Δ . At a finite inverse temperature, β , the symmetry $G(\beta - \tau) = G(\tau)$ of a bosonic function implies the form

$$G(\tau) = a \cosh[(\beta/2 - \tau)\Delta], \quad (\text{S15})$$

where a is a constant.

Even beyond the single-mode case, this form can in principle always be used to extract the gap of a finite system, where the spectrum is a sum of δ -functions, by fitting to the long-time part of $G(\tau)$ where the lowest-energy delta function dominates the decay. If the spectral weight of the lowest δ -function, which by definition is exactly at the gap Δ , is sufficiently large and the second gap to the following δ -function is also sufficiently large, the asymptotic form of $G(\tau)$ is also given by the form of Eq. (S15) if β is sufficiently large. The gap may then be extracted by fitting the large- τ data. In practice, these conditions can be hard to fulfill rigorously, and it becomes necessary to go beyond the single-mode form by performing a fit to more than one exponential, or to perform a still more sophisticated analysis of the long-time decay of the correlation functions. Some methods for this task have been discussed recently [34, 35].

Figure S1 shows two examples of spin correlation functions from the double-cubic Heisenberg model. In Fig. S1(a), the system is well inside the QD phase, the spectrum at $\mathbf{q} = (\pi, \pi, \pi, \pi)$ is completely dominated by a single triplon mode, and it is easy to extract the gap by fitting to Eq. (S15). By contrast, in Fig. S1(b) the system lies in the AFM phase, close to the QCP, where there is significant finite-temperature broadening of the Goldstone mode, which appears at an energy proportional to $1/N$, while the amplitude mode causes further spectral weight to appear at higher energies. In this case it is very difficult to extract the gap by single-mode fitting and a different technique is required to obtain $A(\omega)$; Fig. S2 showed the results obtained by using SAC of the correlation functions of Fig. S1 for this purpose.